



HAL
open science

Coherence gate shaping for wide field high-resolution in vivo retinal imaging with full-field OCT

Pedro Mecê, Kassandra Groux, Jules Scholler, Olivier Thouvenin, Mathias Fink, Kate Grieve, Claude Boccara

► **To cite this version:**

Pedro Mecê, Kassandra Groux, Jules Scholler, Olivier Thouvenin, Mathias Fink, et al.. Coherence gate shaping for wide field high-resolution in vivo retinal imaging with full-field OCT. *Biomedical optics express*, 2020, 11 (9), pp.4928. 10.1364/boe.400522. hal-02988113

HAL Id: hal-02988113

<https://hal.sorbonne-universite.fr/hal-02988113v1>

Submitted on 4 Nov 2020

HAL is a multi-disciplinary open access archive for the deposit and dissemination of scientific research documents, whether they are published or not. The documents may come from teaching and research institutions in France or abroad, or from public or private research centers.

L'archive ouverte pluridisciplinaire **HAL**, est destinée au dépôt et à la diffusion de documents scientifiques de niveau recherche, publiés ou non, émanant des établissements d'enseignement et de recherche français ou étrangers, des laboratoires publics ou privés.



Coherence gate shaping for wide field high-resolution *in vivo* retinal imaging with full-field OCT

PEDRO MECÊ,^{1,*}  KASSANDRA GROUX,¹ JULES SCHOLLER,¹
OLIVIER THOUVENIN,¹  MATHIAS FINK,¹ KATE GRIEVE,^{2,3} AND
CLAUDE BOCCARA¹

¹Institut Langevin, ESPCI Paris, CNRS, PSL University, 1 rue Jussieu, 75005 Paris, France

²Institut de la Vision, Sorbonne Université, INSERM, CNRS, F-75012, Paris, France

³Quinze-Vingts National Eye Hospital, 28 Rue de Charenton, Paris, 75012, France

*pedro.mece@espci.fr

Abstract: Allying high-resolution with a large field-of-view (FOV) is of great importance in the fields of biology and medicine, but it is particularly challenging when imaging non-flat living samples such as the human retina. Indeed, high-resolution is normally achieved with adaptive optics (AO) and scanning methods, which considerably reduce the useful FOV and increase the system complexity. An alternative technique is time-domain full-field optical coherence tomography (FF-OCT), which has already shown its potential for *in-vivo* high-resolution retinal imaging. Here, we introduce coherence gate shaping for FF-OCT, to optically shape the coherence gate geometry to match the sample curvature, thus achieving a larger FOV than previously possible. Using this instrument, we obtained high-resolution images of living human photoreceptors close to the foveal center without AO and with a $1\text{ mm} \times 1\text{ mm}$ FOV in a single shot. This novel advance enables the extraction of photoreceptor-based biomarkers with ease and spatiotemporal monitoring of individual photoreceptors. We compare our findings with AO-assisted ophthalmoscopes, highlighting the potential of FF-OCT, as a compact system, to become a routine clinical imaging technique.

© 2020 Optical Society of America under the terms of the [OSA Open Access Publishing Agreement](#)

1. Introduction

Owing to the optical properties of the eye, the retina is the only part of the central nervous system that can be visualized non-invasively *in-vivo* with micrometer resolution, a crucial aspect for studying neuronal activity [1,2]. Due to their capacity to correct for static and dynamic ocular aberrations [3,4], AO ophthalmoscopes have become the primary technique to image individual retinal neurons such as cone and rod photoreceptors in the living human retina [5–8]. Imaging individual retinal neurons *in-vivo* with AO ophthalmoscopes has enabled new insights into retinal function [2] and a better understanding of progression of retinal diseases such as age-related macular degeneration [9]. However, AO systems require quite complex, expensive and cumbersome hardware, limiting their clinical and commercial deployment [10,11]. Moreover, the eye's isoplanatic patch (around 0.6 mm) limits the useful field-of-view (FOV) where high-resolution retinal imaging can be achieved when using AO [12]. Although multi-conjugate AO was demonstrated in order to achieve a larger useful FOV, increasing the eye's isoplanatic patch, this solution adds complexity, as two deformable mirrors are necessary [13]. Thus, achieving cellular resolution in a large portion of the living human retina without using AO is of great interest.

Recent studies have achieved high-resolution retinal imaging without using AO by implementing computational ocular aberration correction [11,14–17]. Although promising, these approaches only presented results in far foveal eccentricities (3° or more), where photoreceptors are most

easily resolved. Moreover, they require heavy post-processing steps hence providing limited feedback during imaging sessions, and, in some cases, expensive hardware was also necessary (e.g. a very fast camera and/or swept source laser). The use of a super-resolution optical-reassignment technique was also proposed as a tool to achieve cellular resolution in in-vivo retina without AO [18]. Nevertheless, a scanning illumination/detection is used, presenting an inherently low frame rate, limited FOV (lower than $0.3 \text{ mm} \times 0.3 \text{ mm}$) and high sensitivity to fixational eye motion [19] leading to intraframe distortion.

An alternative modality to achieve high-cellular resolution without using AO is FF-OCT, which uses a spatially incoherent light source, a high-speed megapixel camera and time-domain phase modulation to acquire *en-face* sections of the sample at a given depth [20]. One attractive point of this technique for retinal imaging is the fact that the optical resolution of FF-OCT has a weak sensitivity to predominant ocular aberrations (i.e. defocus and astigmatism) [21–23]. This interesting feature was recently highlighted in [24], where *in-vivo* human cone mosaic at eccentricities close to the fovea was resolved. Although FF-OCT's FOV is theoretically only limited by the spatial sampling of the imaging camera, retinal curvature causes current images to have a limited useful FOV of about $0.4 \text{ mm} \times 0.4 \text{ mm}$ [24,25].

Typically, FF-OCT uses a Linnik interferometer, where identical microscope objectives are placed in both reference and sample arms in a symmetric optical path configuration. When applied to retinal imaging, the FF-OCT symmetry is broken, as the sample arm no longer contains a microscope objective (Fig. 2), but rather contains the anterior segment optics of the human eye. Here, we theoretically and experimentally demonstrate that when the symmetry is broken a curved coherence gate is generated, provoking a mismatch with the retinal curvature, and consequently limiting the useful FOV. The useful FOV can be defined as the FOV over which a structure from a given depth of the sample can be visualized. We present novel advances in FF-OCT allowing for optical shaping of the geometry of the coherence gate, adapting it to the retinal geometry, enabling the generation of single-shot, high-resolution, wide FOV images ($1 \text{ mm} \times 1 \text{ mm}$) of the photoreceptor mosaic as close as 1° from the foveal center. The $1 \text{ mm} \times 1 \text{ mm}$ useful FOV is 6.25 times larger in this new configuration compared to our previous results [24]. Then, we show that useful tools to diagnose retinal disorders at the early stage such as photoreceptor-based biomarkers and spatiotemporal monitoring of individual photoreceptors can be achieved without the need for AO.

2. Methods

2.1. Theory

The optical path length (OPL) when light propagates in a material x of thickness e_x , refractive index n_x for a given angle θ_x can be expressed as:

$$OPL(\lambda) = \sum_{x=1}^N n_x(\lambda) \frac{e_x}{\cos\theta_x}. \quad (1)$$

Where $n_x(\lambda)$ is given by the Sellmeier equation [26]. The incidence angle in a material x , θ_x , can be expressed as a function of the incidence angle in air θ_1 , as follows:

$$\theta_x = \sin^{-1} \left(\frac{\sin\theta_1}{n_x(\lambda)} \right). \quad (2)$$

Through Eqs. (1) and (2), one can notice the dependency of the OPL on the wavelength (λ) and the incidence angle in air (θ_1):

$$OPL(\lambda, \theta_1) = \sum_{x=1}^N n_x(\lambda) \frac{e_x}{\cos \left(\sin^{-1} \left(\frac{\sin\theta_1}{n_x(\lambda)} \right) \right)}. \quad (3)$$

The depth position of the *en-face* image generated by the FF-OCT, *i.e.* the coherence gate, is given by the the optical path difference (OPD) between the reference and sample arms:

$$OPD(\lambda, \theta_1) = OPL_{reference}(\lambda, \theta_1) - OPL_{sample}(\lambda, \theta_1). \quad (4)$$

If the OPL of both arms is symmetric, as is the case when a microscope objective is placed in each arm, the OPD is null for all values of θ_1 , *i.e.* in the FOV. On the other hand, an asymmetry between the reference and sample OPLs creates a dependency on the the wavelength (λ) and the incident angle in the air (θ_1). In this case, OPD would only be null for a given incident angle, and it would increase as this angle is increased. This is the origin of the curvature of the coherence gate.

To shape the coherence gate geometry, we propose the use of optical windows. To better understand how optical windows can shape the coherence gate geometry, we can consider a typical FF-OCT set-up composed of identical microscopic objectives positioned in each arm, with an optical window of thickness e_b and refractive index n_b positioned in the sample arm (Fig. 1). For simplicity, we assume that both arms are illuminated with monochromatic light.

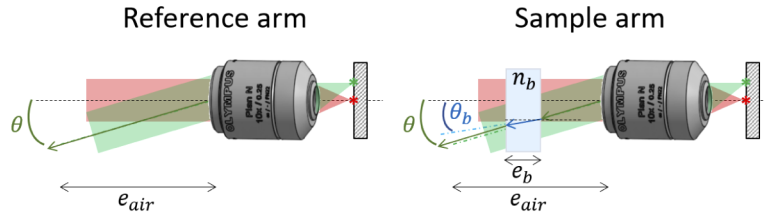


Fig. 1. Schematic of the reference and sample arms introducing notations for the OPD model.

Their respective OPLs will be given as follows (only considering the path between the microscope objective and the beam splitter):

$$OPL_{ref}(\theta) = \frac{e_{air}}{\cos(\theta)} \quad (5)$$

$$OPL_{sample}(\theta) = \frac{e_{air} - e_b}{\cos(\theta)} + \frac{e_b n_b}{\cos(\theta_b(\theta))} \quad (6)$$

where θ_b is given as a function of the incident angle in the air θ according to Eq. (2). In this case, the OPD would be:

$$OPD(\theta) = e_b \left(\frac{n_b}{\cos(\theta_b(\theta))} - \frac{1}{\cos(\theta)} \right). \quad (7)$$

To image at a depth of interest of the sample, one has to move the reference arm. We can move the reference arm in order to match both OPLs for a given angle, for example at a central point in the FOV, *i.e.* $\theta = 0$, which gives:

$$OPD(0) = e_b(n_b - 1). \quad (8)$$

Now, the OPD for all the other angles θ will be given by:

$$OPD(\theta) = e_b \left(\frac{n_b}{\cos(\theta_b(\theta))} - \frac{1}{\cos(\theta)} \right) - e_b(n_b - 1) \quad (9)$$

which can be simplified as follows:

$$OPD(\theta) = e_b \left(n_b \frac{1 - \cos(\theta_b(\theta))}{\cos(\theta_b(\theta))} - \frac{1 - \cos(\theta)}{\cos(\theta)} \right). \quad (10)$$

Note that the introduction of an optical window induces a variation of the OPD as a function of the FOV, generating a curved coherence gate.

2.2. Experimental setup

To investigate the impact of the asymmetric Linnik interferometer configuration on coherence gate curvature, three samples were imaged: 1) a standard USAF resolution target; 2) an OEMI-7 model eye (Ocular Instruments, Inc) which takes into account the eye geometry, optical power and dispersion properties (henceforth, named model eye); and 3) *in-vivo* human retina. Figure 2 presents the schematic of the custom-built FF-OCT system coupled through a dichroic mirror with a Thorlabs Ganymede-II SD-OCT system. The FF-OCT comprises a light-emitting diode (LED) with $\lambda = 850$ nm center wavelength and 30 nm bandwidth (M850L3, Thorlabs), used as a spatially incoherent illumination source, giving a theoretical axial resolution of approximately $8 \mu\text{m}$ in water. The LED is focused by a condenser lens 20 mm in front of the eye's pupil. A physical diaphragm is positioned in front of the LED, conjugate to the retina and the FF-OCT reference mirror. The illumination beam is split into reference and sample arms by a 50:50 cubic beam splitter (BS). For the reference arm, an Olympus 10X/0.25 NA Plan Achromat objective is used with a silicon mirror placed at the focal plane of the objective. The whole reference arm (microscope objective and silicon mirror) is mounted on a fast voice-coil translation stage (X-DMQ12P-DE52, Zaber Technologies Inc.), enabling adjustment of the coherence gate position. For the sample arm, two configurations were used. In the case of the USAF target imaging, a microscope objective, identical to the one used in the reference arm, is used leading to a symmetric Linnik configuration (not shown in Fig. 2). In the case of the model eye and *in-vivo* retinal imaging, both were aligned along the optical axis, without the use of a microscope objective, leading to an asymmetric Linnik configuration (shown in Fig. 2). The FF-OCT light beam arrives with an 8 mm diameter in the eye's pupil. The back-scattered photons from both arms are recombined by the same BS and focused onto a high-speed (up to 720 Hz at 1440×1440 pixel) CMOS camera (Q-2A750-Hm/CXP-6, Adimec) for FF-OCT imaging. The FF-OCT system aperture was limited by the eye's pupil. In the case of *in-vivo* retinal imaging, the SD-OCT and the voice-coil translation stage were used to measure and correct for involuntary axial eye movements during the imaging acquisition in a closed-loop fashion [24]. The SD-OCT light beam was filtered out from the FF-OCT reference and detection arms by using a short-pass filter (FESH0850 25mm aperture, Thorlabs).

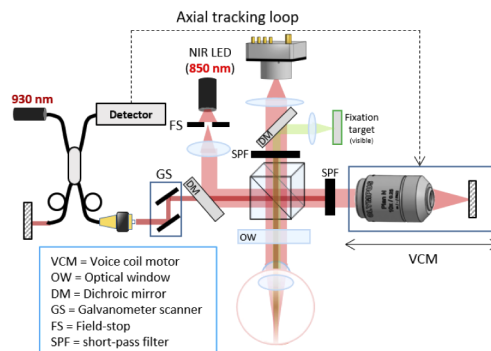


Fig. 2. Schematic drawing of the custom-built FF-OCT system coupled with an SD-OCT for real-time axial motion correction and FF-OCT coherence gate positioning guidance. In the case of the USAF target imaging, a microscope objective, identical to the one used in the reference arm, is used leading to a symmetric Linnik configuration (not shown in the schematic). In the case of the model eye and *in-vivo* retinal imaging, no microscope objective is placed in the sample arm, leading to an asymmetric Linnik configuration (shown in the schematic).

2.3. Image acquisition

In the case of the USAF target and the model eye imaging, a total of 200 images from different depths were acquired at 10 Hz, by moving the voice-coil translation stage of the reference arm at a constant speed of $5 \mu\text{m/s}$. This procedure allowed us to acquire *en-face* images from different depths, forming Z-stacks. This procedure was repeated after adding optical windows of N-BK7 of different thicknesses in the reference or sample arms in order to change the geometry of the coherence gate.

In the case of *in vivo* retinal imaging, the image acquisition was performed on two healthy subjects S1 and S2 aged 25 and 30 respectively. S1 presents a refractive error of $1.5D \times 0.5D \times 160^\circ$ (spherical \times cylindrical \times axis of cylindrical errors), S2 does not wear prescribed eyeglasses and had had LASIK refractive surgery several years ago. Research procedures followed the tenets of the Declaration of Helsinki. Informed consent was obtained from subjects after the nature and possible outcomes of the study were explained. The study was authorized by the appropriate ethics review boards (CPP and ANSM (IDRCB number: 2019-A00942-55)). Subjects were seated in front of the system and stabilized with a chin and forehead rest and asked to fixate a target placed at an infinite focal conjugate. During the imaging session, the subject S1 was wearing her prescription glasses to increase the signal level of FF-OCT [23]. Image acquisition was realized in a dark room, maximizing the pupil dilation. Phase modulation was performed by the residual axial motion after optical stabilization [24]. Image sequences were composed of 150 frames acquired at 300 Hz using custom-built software. The FF-OCT camera worked close to saturation to use the whole full well capacity, decreasing relative importance of shot noise [27]. During image acquisition, the total power entering the eye from the FF-OCT illumination source and the SD-OCT scanning source were respectively 1.3 mW (for the 0.5 s of image acquisition) and 0.25 mW (continuous scanning), which are below the ocular safety limits established by the ISO standards for group 1 devices.

2.4. Image processing

In the case of the USAF target and the model eye imaging, each Z-stack was digitally converted into axial sections, *i.e.* a cross-sectional view of the sample. This step was possible by taking into account only the pixels of a central row of each image. Next, image segmentation was applied using an intensity-based thresholding algorithm and a least square parabola fitting algorithm, enabling measurement of the degree of curvature of converted cross-sections.

For *in-vivo* retinal imaging, each image was normalized by dividing itself by its mean value. Since the phase was randomly modulated by the residual tracking error, and to eliminate the incoherent terms, we adopted a 2-phase demodulation [24]. The 2-phase demodulation consists of subtracting one image I_N from the next I_{N+1} and taking the absolute value. Next, images with a very low or absent useful signal, mainly due to an insufficient phase shift between consecutive images, were automatically detected using an intensity-based threshold algorithm, and then excluded from the image sequence. Finally, useful images were registered using a custom-built normalized cross-correlation algorithm, where the image presenting the highest signal level was chosen as the reference. Retinal images of subject S1 were also acquired using the rtx-1 adaptive optics flood-illumination ophthalmoscope (AO-FIO - Imagine Eyes, France) and the MAORI confocal adaptive optics scanning-laser ophthalmoscope (AO-SLO - Physical Sciences, Inc, Andover, MA, USA). Retinal fundus images of both subjects were also acquired with Spectralis scanning-laser ophthalmoscope (SLO) (Heidelberg Engineering, Germany). All images were acquired in the same conditions as previously described, *i.e.* in a dark room, maximizing the pupil dilation and with subject S1 wearing her prescribed eyeglasses. To generate a pointwise density map, we divided the cone mosaic image into an overlapping grid of 300×300 pixels (corresponding to $200 \mu\text{m} \times 200 \mu\text{m}$) regions of interest (ROIs), where each ROI was displaced from the previous by 30 pixels (corresponding to $20 \mu\text{m}$). These values were chosen empirically

to provide a good trade-off between pointwise accuracy and map smoothness. Then, cone density and spacing were computed for each ROI using a fully automated algorithm based on modal spacing as described in [28]. Bicubic image interpolation was used to increase the size of the cone density map in order to match the cone mosaic image.

3. Results

3.1. Optical shaping of the coherence gate geometry

Figure 3 shows how the coherence gate geometry can be optically shaped by adding optical windows in one of the interferometer arms. When imaging the USAF target (Fig. 3(a)) in a symmetric configuration the cross-section looks completely flat. The addition of an optical window in one of the arms breaks this symmetry, consequently, the flat sample presents an apparent curved cross-section. This apparent curvature happens because of a non-constant optical path difference along the FOV, generating a curved coherence gate.

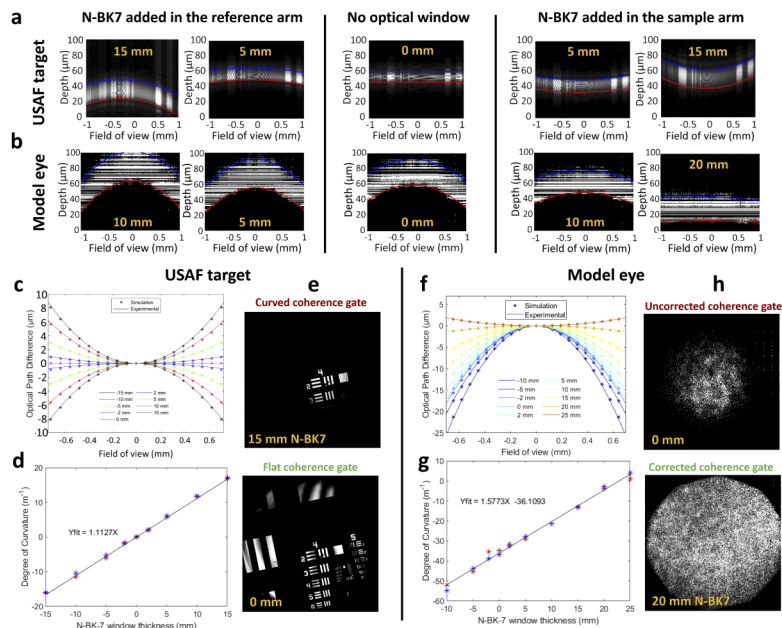


Fig. 3. **a-b**, Cross-sections after introducing N-BK7 optical windows with various thicknesses (in yellow) in the reference or sample arms when imaging, respectively, the USAF target and the model eye. **c,d,f,g**, Measured and theoretical optical path differences as a function of the FOV for different optical window thicknesses, as well as their respective degree of curvature, for respectively the USAF target and the model eye. When the optical window was introduced in the reference arm, the N-BK7 optical window thickness was represented in negative value. **e,h**, The effect of the coherence gate geometry over the FF-OCT useful FOV.

Figure 3(c) presents the measured and the theoretical (see Sect. 2.1) OPDs as a function of the FOV. Depending on which arm the optical window is introduced in, the coherence gate curvature can present a concave or a convex shape. One can notice that the curvature increases as a function of the thickness of the optical window introduced in one of the arms (Fig. 3(d)). The induced curvature of the coherence gate directly impacts the useful FOV of an FF-OCT system, since it acquires *en-face* curved sections of a flat sample at a given depth (Fig. 3(e)).

The same experiment can be done now using the model eye, which presents similar geometry and dispersion of the eye, in an asymmetric configuration (Fig. 3(b)). In this case, already when no optical window is introduced, the coherence gate presents a significant curvature. Figures 3(f,g) give the measured and theoretical curvature as a function of the FOV and the optical window thickness. The introduction of an 20 mm thick N-BK7 optical window in the sample arm enables compensation for the initial apparent curvature, increasing the useful FOV (Fig. 3(h)). [Visualization 1](#), [Visualization 2](#), [Visualization 3](#), and [Visualization 4](#) show acquired Z-stacks for curved and flat coherence gate when imaging the USAF target and the model eye.

3.2. Living human retinal cone mosaic imaging

Figures 4(a,b) presents *in-vivo* retinal images from the inner/outer segment junction (IS/OS) of subject S1 before and after compensation of the coherence gate curvature respectively. The yellow square in the retinal fundus image (Fig. 4(c)) indicates the location of acquired images, *i.e.* as close as 1° from the foveal center. According to Fig. 3(g), by adding an N-BK7 optical window with 20mm thickness, the coherence gate curvature would be strongly minimized. With this configuration, we obtained a high-resolution foveal cone mosaic imaging with a useful FOV of $1\text{ mm} \times 1\text{ mm}$, larger than the previous FOV ($0.4\text{ mm} \times 0.4\text{ mm}$) [24] by a factor of 6.25, only correcting ocular aberrations with prescribed eyeglasses. Zoomed areas and their respective power spectral densities (PSD) are also presented. All PSDs presented Yellot's ring, the spectral signature of the photoreceptor mosaic image [29].

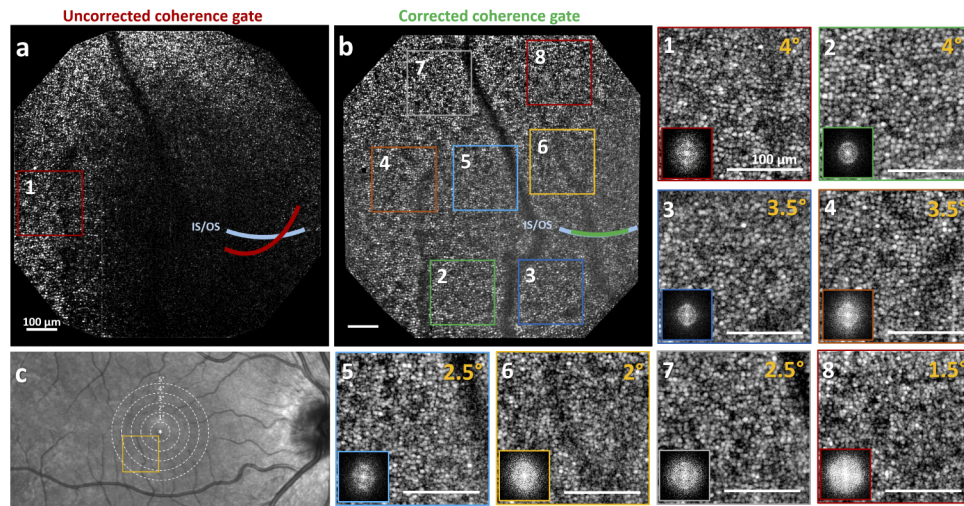


Fig. 4. Foveal cone mosaic images of subject S1 as close as 1° from the foveal center (yellow square of the retinal fundus image). **a,b**, Respectively, acquired images from the IS/OS junction before and after correcting for the coherence gate curvature. Zoomed areas, and their respective eccentricity (in yellow) and PSD are also presented. All PSDs present the Yellot's ring [29]. Scale bar, $100\mu\text{m}$.

Figure 5 presents cone mosaic images obtained for subject S2 at 3° eccentricity temporal to the fovea after correcting the coherence gate curvature. Cone photoreceptors can also be resolved in the whole $1\text{ mm} \times 1\text{ mm}$ FOV. Note that the same 20 mm thick N-BK7 optical window used for S1 is also suitable to correct the coherence gate curvature for S2.

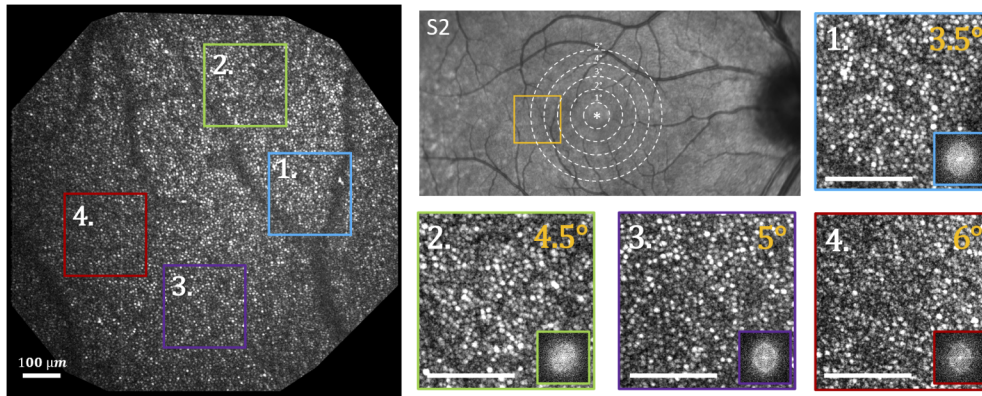


Fig. 5. Foveal cone images of subject S2 after correcting the coherence gate curvature. Zoomed areas, and their respective eccentricity (in yellow) and PSD are also presented. Scale bar, $100\mu\text{m}$.

3.3. Photoreceptor-based biomarkers and 4D monitoring of individual photoreceptors

The compensation of the coherence gate curvature enables the visualization of photoreceptors in the whole FOV. Consequently, we can obtain important information on photoreceptor-based biomarkers such as distribution, density, and spacing within a few seconds in a single-shot (no image montaging is necessary) with ease (Fig. 6). All measurements are consistent with histology and AO-assisted cone density measurement [30,31].

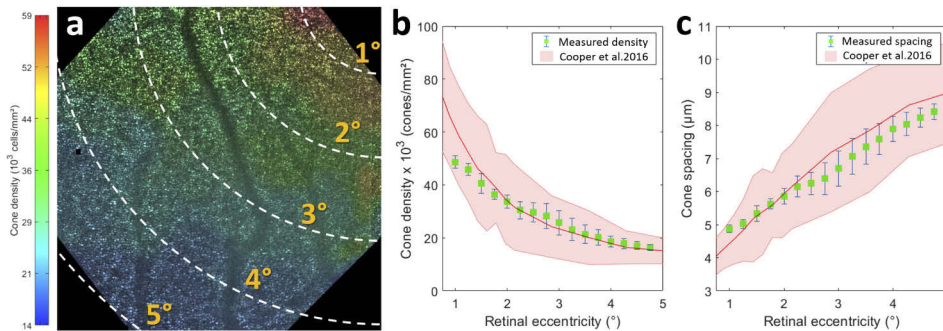


Fig. 6. **a**, Cone density distribution color coded for the image acquired from subject S1. **b-c**, Respectively, mean (green squares) and standard deviation (blue lines) of the measured cone density and spacing as a function of the retinal eccentricity. The red line is the mean computed density and the shaded region is 95% prediction interval obtained from a dataset of a 20-eye healthy population using an AO scanning-laser ophthalmoscope [31].

Minimizing the effect of the coherence gate curvature also helps to increase the repeatability of the imaging, allowing for spatiotemporal monitoring of individual photoreceptors. [Visualization 5](#) presents four image sequences acquired in the same region with a 10 min interval between acquisitions. Note in zoomed areas that individual photoreceptors can be tracked frame-by-frame (3 ms interval) and video-by-video (10 min interval). Green boxes highlight cones that are visible in all four videos, while yellow boxes highlight those visible for only some of the videos, which might indicate a long-term change of reflectivity [32]. Red hexagons highlight the typical pattern found in cone mosaic close to the fovea [30]. Figure 7(a-d) presents the averaged image obtained from zoomed areas of [Visualization 5](#). Figures 7(e-h) and [Visualization 6](#) and

Visualization 7 show a cone-to-cone comparison of FF-OCT image with images generated by two AO ophthalmoscope modalities for subject S1 at same location. FF-OCT allows visualization of most, if not all, photoreceptors identified in AO-assisted images. Note in Fig. 7(i) that PSDs from all FF-OCT images present a clear and well-defined cone mosaic spatial frequency (vertical pale red bar) at 120 cycles/mm, as is the case for both AO-assisted imaging modalities. On the other hand, when using a scanning laser ophthalmoscope without closing the AO-loop, an erroneous spatial frequency is measured, leading to an error in cone density computation.

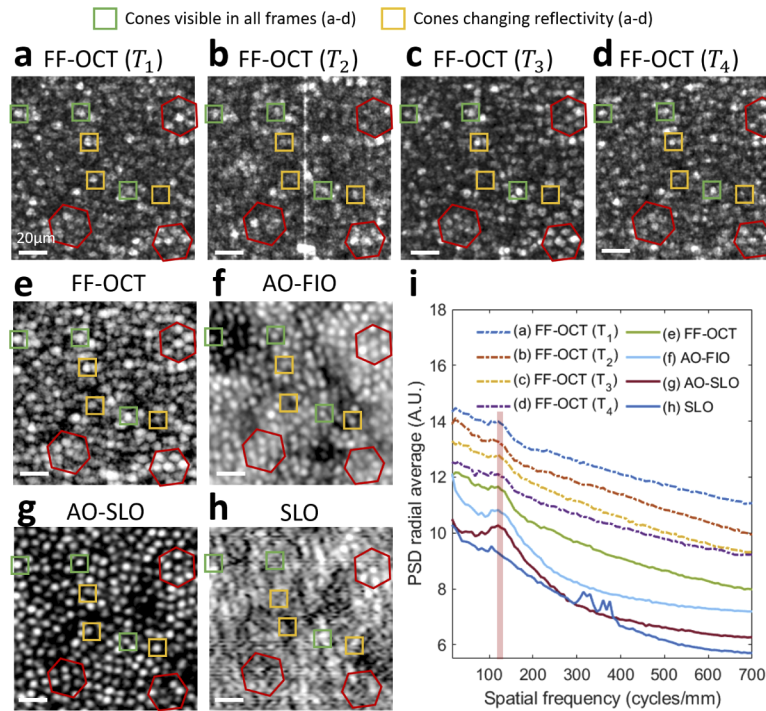


Fig. 7. **a-d**, Cone mosaic images acquired at the same region (4.5° eccentricity) for different time points $T_{1,2,3,4}$, with 10 minutes interval between acquisitions, for subject S1, highlighting the capacity of FF-OCT with coherence gate shaping to track individual cones in space and time. Green boxes: cones visible for all four acquisitions. Yellow boxes: cones changing reflectivity. Red hexagons: pattern found in cone mosaic close to the fovea [30]. **e**, Cone mosaic image obtained after averaging images from **a-d**. **f-h**, Cone mosaic image at the same region acquired using AO-ophthalmoscopes. **f**, FIO: Flood-illumination ophthalmoscope. **g**, SLO: confocal scanning-laser ophthalmoscope. **h**, Acquisition made without closing the AO-loop. **i**, PSD radial average for images **a-h**, where the vertical pale red bar outlines the expected cone mosaic spatial frequency. PSDs were vertically displaced for better visualization. Scale bar, $20 \mu\text{m}$.

4. Discussion

In this paper, we saw that the Linnik symmetry plays an important role in obtaining a flat coherence gate. Although this symmetry is broken in the case of retinal imaging, inducing an intrinsically curved coherence gate, we showed that the coherence gate geometry can be corrected by introducing a simple optical element such as an optical window into one of the interferometer arms. We used this technique to compensate the intrinsic curved coherence gate in the asymmetric configuration of FF-OCT for retinal imaging, obtaining an useful FOV of

1 mm × 1 mm, limited only by the size and the spatial sampling of the imaging camera. To the best of our knowledge, this is the first OCT system allying a FOV as large as 1 mm × 1 mm, high spatial resolution in all three dimensions and high acquisition rate of a given retinal plane (up to 300 Hz), without using any optical or digital aberration compensation other than prescribed eyeglasses, considerably simplifying the hardware and software complexity. The coherence gate curvature was previously reported for scanning-like OCT, mainly linked to the scanning-induced path length variation in non telecentric optical systems [33]. Therefore, the described method to optically shape the coherence gate can also be applied in OCT and Optical Coherence Microscopy imaging techniques to avoid curvature artefacts and to compensate for optical components that are only positioned in one of the arms, inducing an asymmetry.

Another expected effect brought by the asymmetry of the Linnik interferometry is dispersion, affecting the axial resolution of the FF-OCT (*i.e.* axial sectioning capacity). This phenomenon can be noted in cross-sections of Figs. 3(a,b) as an increase of the coherence gate thickness (distance between the blue and red curves). Figure 8 shows the FWHM of the coherence gate thickness (FF-OCT axial resolution) as a function of the optical window thickness in the case of the USAF target imaging (in red) and the model eye imaging (in blue). Note that for the USAF target imaging, a flat coherence gate coincides with the best axial sectioning capability, both happening when no optical window is added (symmetric configuration). In the case of the model eye imaging, not surprisingly, the optimum correction of dispersion does not coincide with the optimum correction of coherence gate curvature, since these two phenomena have different physical origins.

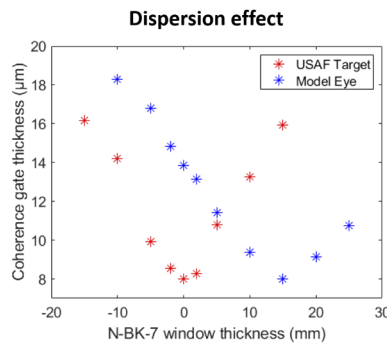


Fig. 8. Experimental data from Fig. 3 showing how dispersion evolves for different thicknesses of optical windows. The FWHM of the coherence gate thickness (FF-OCT axial resolution) as a function of the optical window thickness in the case of the USAF target (red points) and model eye (blue points) imaging respectively.

An optimum compensation of the coherence gate curvature would be possible with a 22 mm N-BK7 optical window (Fig. 3(g)). Figure 8 shows, for the model eye imaging, that an optimum dispersion compensation would be possible with a 15 mm of N-BK7 optical window. In this study, in order to compromise and minimize the effects of both curvature of the coherence gate and dispersion for *in-vivo* retinal imaging, we used a N-BK7 optical window with 20 mm thickness. According to Fig. 3(g) and Fig. 8, a good trade-off could be found in this case: the axial resolution would be around 9 μm, instead of 8 μm, and the degree of curvature would be lower than 5, meaning an edge-center difference of 1 μm.

We presented results in two different subjects presenting different refractive errors at two different retinal eccentricities. In both cases, a 20-mm thick N-BK7 optical window was suitable to achieve a 1 mm × 1 mm FOV. Indeed, since the axial resolution is around 9 μm, a mismatch between the coherence gate geometry and the retina curvature inferior to the optical sectioning (given by the FF-OCT axial resolution) would not be seen (Fig. 9(a-c)). Figure 9(d) shows

theoretical degree of curvature values, validated by our previous model (Sect. 2.1 and Fig. 3(c,f)), for different eye lengths. One can see that a 20-mm thick N-BK7 optical window would be suitable (edge-center distance inferior to $1\mu\text{m}$) to achieve a $1\text{ mm} \times 1\text{ mm}$ FOV for eye lengths varying from 20 mm to 28 mm, which covers the majority of cases in the population [34]. It is therefore not necessary to swap optical window for each subject: the 20mm thick window covers the whole range of eye lengths that one would typically see in the clinic.

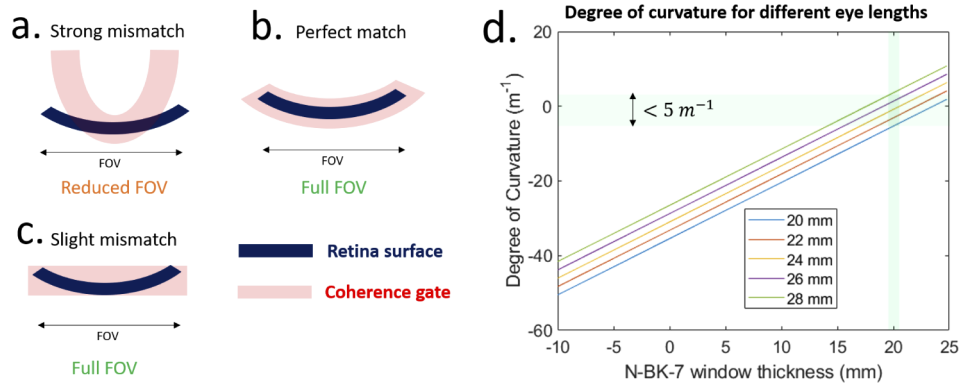


Fig. 9. (a-c) Schematic showing different degrees of curvature for the coherence gate and their consequence on the FOV of the FF-OCT image. Although the coherence gate curvature does not perfectly match the retinal curvature in the case of (c), a full FOV is still generated, as the coherence gate has a given thickness defined by the axial resolution. (d) Expected theoretical value of degree of curvature (computed using Eq. (1)) as a function of the thickness of the N-BK7 introduced to compensate for coherence gate curvature for different eye lengths. Green shaded area highlights that a N-BK7 of 20 mm thickness covers the majority of eye lengths in the population (from 20 mm to 28 mm) [34].

In this study, we only considered N-BK7 optical windows to minimize effects of both coherence gate curvature and dispersion. Another solution to optically shape the geometry of the coherence gate is the introduction of a deformable reference mirror in the reference arm. This solution would decouple the correction of the coherence gate curvature and dispersion, since a suitable optical window in the sample arm could compensate for dispersion effect and the deformable reference arm would correct the residual curvature of the coherence gate, without affecting dispersion, improving signal level, axial resolution and possibly achieving even larger FOV. Moreover, this solution might extend the coherence gate shaping to samples with an irregular surface, more complex than a curvature, such as deformed retina due to degeneration, detachment, etc. In the case of imaging a deformed retina, a deformable reference would enable imaging an irregular retinal layer over a large FOV in a single shot instead of acquiring *en-face* images for different coherent plane positions. Nevertheless, the main drawback of this solution is the considerable increase of the system complexity and cost, making clinical transfer challenging. A solution considering only a 20 mm thick N-BK7 optical window, as presented in this paper, seems suitable to minimize both curvature of the coherence gate and dispersion for a large population.

The direct visualization of individual photoreceptors together with photoreceptor-based biomarkers, such as distribution, density and spacing, could be useful tools to diagnose retinal disorders at the early stages, in order to monitor retinal disease progression as well as the effect of potential therapeutic interventions [32]. The presented FF-OCT system with coherence gate shaping enables 4D monitoring of individual photoreceptors and photoreceptor-based biomarkers with good accuracy and repeatability in a wide FOV, without image distortion (due to eye motion) and long, fastidious acquisition sessions to cover the retinal area of interest, as is the case with

lab-built scanning systems with limited FOV such as AO-SLO and AO-OCT. While AO-FIO can achieve $1\text{ mm} \times 1\text{ mm}$ FOV at a high-frame rate [8], high-resolution brought by ocular aberration correction using AO is limited by the eye's field aberrations, commonly known as the isoplanatic patch [12], affecting the accuracy of the resultant photoreceptor-based biomarkers. This issue can be tackled by limiting the system aperture (around 5 mm in the eye's pupil plane), provoking a decrease of resolution and signal-to-noise ratio (SNR), as rtx-1 (Imagine Eyes, France) and [8]; or by using multi-conjugated AO, with an increased system complexity as a second deformable mirror is necessary [13]. The present FF-OCT with coherence gate shaping can resolve photoreceptor and extract photoreceptor-based biomarkers in the whole FOV without AO, considerably decreasing the system complexity and footprint, which may help clinical deployment. Additionally, FF-OCT has the capacity to generate en-face retinal images with an enhanced axial resolution ($9\ \mu\text{m}$) compared to confocal AO-SLO (around $40\ \mu\text{m}$ [35]) and AO-FIO (no inherent optical sectioning). This advantage can be observed in Fig. 7, especially in comparison with AO-FIO, where a structured background can be observed in the latter, probably coming from the choroid positioned beneath the photoreceptor layer, which is completely filtered out by the FF-OCT thanks to its high axial resolution. Although FF-OCT axial resolution may be slightly poorer than AO-OCT [10], it has advantages of larger FOV, higher-frame rate and lower complexity and size, and is still able to resolve the photoreceptor interfaces such as IS/OS junction and cone outer segment tips. Moreover, the high temporal resolution of FF-OCT may play an important role to characterize the temporal behavior of retinal capillaries from different plexus [36,37] and the temporal dynamics of subcellular structures [27]. Finally, although FF-OCT is only weakly sensitive to low-order ocular aberrations in terms of resolution, aberrations still reduce the FF-OCT signal level [38]. Ocular aberrations may explain why the SNR of FF-OCT images varies across the FOV (Figs. 4 and 5) and why the AO-SLO image has higher contrast than the FF-OCT image (Fig. 7). Although the presented imaging technique presents lower SNR compared to AO-SLO, photoreceptors can still be visualized in single unaveraged frames, as it was demonstrated in Visualization 5, and photoreceptor-based biomarkers can still be extracted with accuracy (Fig. 6).

5. Conclusion

In conclusion, we have developed coherence gate shaping for FF-OCT to adapt coherence gate geometry to the curvature of the sample being imaged, making large FOV imaging possible while keeping high-resolution in samples under constant motion, such as the living human eye. We applied this method to achieve, in a single shot, and without the use of AO, $1\text{ mm} \times 1\text{ mm}$ FOV image of the living human cone mosaic as close as 1° from the foveal center. We showed that a large FOV allied with a high resolution in all three dimensions, brings a significant benefit for retinal imaging: the large FOV facilitates the localization of the region of interest, allows a global interpretation of the retinal condition over this area, such as cone density distribution, and drastically reduces the image session duration; the high resolution allows tracking of individual cones and computation of cellular information, such as cell density and spacing, that could be used as biomarkers to diagnose retinal disorders at early stages. FF-OCT with improved performance thanks to coherence gate shaping may pave the way towards its adoption as a routine clinical imaging system, helping to understand retinal structure and disease.

Funding

European Research Council (610110); Conseil Régional, Île-de-France (Sesame 4D-EYE EX047007); Centre National de la Recherche Scientifique (Pre-maturation program); Fondation Voir et Entendre (x16-CARN- 0029-01); Agence Nationale de la Recherche (IHU FOReSIGHT ANR-18-IAHU-0001).

Acknowledgments

The authors want to thank Céline Chaumette for helping to acquire SLO and AO-FIO images and Michel Paques and José Sahel for their clinical expertise and support.

Disclosures

P. Mecê: PSL University (P), C. Boccara: PSL University (P), others: none.

References

1. A. London, I. Benhar, and M. Schwartz, "The retina as a window to the brain - from eye research to cns disorders," *Nat. Rev. Neurol.* **9**(1), 44–53 (2013).
2. J. J. Hunter, W. H. Merigan, and J. B. Schallek, "Imaging retinal activity in the living eye," *Annu. Rev. Vis. Sci.* **5**(1), 15–45 (2019).
3. J. Jarosz, P. Mecê, J.-M. Conan, C. Petit, M. Paques, and S. Meimon, "High temporal resolution aberrometry in a 50-eye population and implications for adaptive optics error budget," *Biomed. Opt. Express* **8**(4), 2088–2105 (2017).
4. P. Mecê, E. Gofas-Salas, C. Petit, F. Cassaing, J. Sahel, M. Paques, K. Grieve, and S. Meimon, "Higher adaptive optics loop rate enhances axial resolution in nonconfocal ophthalmoscopes," *Opt. Lett.* **44**(9), 2208–2211 (2019).
5. J. Liang, D. R. Williams, and D. T. Miller, "Supernormal vision and high-resolution retinal imaging through adaptive optics," *J. Opt. Soc. Am. A* **14**(11), 2884–2892 (1997).
6. A. Roorda, F. Romero-Borja, W. J. Donnelly III, H. Queener, T. J. Hebert, and M. C. Campbell, "Adaptive optics scanning laser ophthalmoscopy," *Opt. Express* **10**(9), 405–412 (2002).
7. M. Zacharria, B. Lamory, and N. Chateau, "Biomedical imaging: New view of the eye," *Nat. Photonics* **5**(1), 24–26 (2011).
8. E. Gofas-Salas, P. Mecê, C. Petit, J. Jarosz, L. M. Mugnier, A. M. Bonnefois, K. Grieve, J. Sahel, M. Paques, and S. Meimon, "High loop rate adaptive optics flood illumination ophthalmoscope with structured illumination capability," *Appl. Opt.* **57**(20), 5635–5642 (2018).
9. M. Paques, S. Meimon, F. Rossant, D. Rosenbaum, S. Mrejen, F. Sennlaub, and K. Grieve, "Adaptive optics ophthalmoscopy: Application to age-related macular degeneration and vascular diseases," *Prog. Retinal Eye Res.* **66**, 1–16 (2018).
10. R. S. Jonnal, O. P. Kocaoglu, R. J. Zawadzki, Z. Liu, D. T. Miller, and J. S. Werner, "A review of adaptive optics optical coherence tomography: technical advances, scientific applications, and the future," *Invest. Ophthalmol. Visual Sci.* **57**(9), OCT51–OCT68 (2016).
11. N. D. Shemonski, F. A. South, Y.-Z. Liu, S. G. Adie, P. S. Carney, and S. A. Boppart, "Computational high-resolution optical imaging of the living human retina," *Nat. Photonics* **9**(7), 440–443 (2015).
12. P. Bedggood, M. Daaboul, R. A. Ashman, G. G. Smith, and A. Metha, "Characteristics of the human isoplanatic patch and implications for adaptive optics retinal imaging," *J. Biomed. Opt.* **13**(2), 024008 (2008).
13. M. Laslandes, M. Salas, C. K. Hitzengerger, and M. Pircher, "Increasing the field of view of adaptive optics scanning laser ophthalmoscopy," *Biomed. Opt. Express* **8**(11), 4811–4826 (2017).
14. D. Hillmann, H. Spahr, C. Hain, H. Sudkamp, G. Franke, C. Pfäffle, C. Winter, and G. Hüttmann, "Aberration-free volumetric high-speed imaging of in vivo retina," *Sci. Rep.* **6**(1), 35209 (2016).
15. D. Borycki, E. Aukorius, P. Węgrzyn, and M. Wojtkowski, "Computational aberration correction in spatiotemporal optical coherence (stoc) imaging," *Opt. Lett.* **45**(6), 1293–1296 (2020).
16. L. Ginner, A. Kumar, D. Fechtig, L. M. Wurster, M. Salas, M. Pircher, and R. A. Leitgeb, "Noniterative digital aberration correction for cellular resolution retinal optical coherence tomography in vivo," *Optica* **4**(8), 924–931 (2017).
17. H. Sudkamp, D. Hillmann, P. Koch, M. vom Endt, H. Spahr, M. Münt, C. Pfäffle, R. Birngruber, and G. Hüttmann, "Simple approach for aberration-corrected oct imaging of the human retina," *Opt. Lett.* **43**(17), 4224–4227 (2018).
18. T. B. DuBose, F. LaRocca, S. Farsiu, and J. A. Izatt, "Super-resolution retinal imaging using optically reassigned scanning laser ophthalmoscopy," *Nat. Photonics* **13**(4), 257–262 (2019).
19. P. Mecê, J. Jarosz, J.-M. Conan, C. Petit, K. Grieve, M. Paques, and S. Meimon, "Fixational eye movement: a negligible source of dynamic aberration," *Biomed. Opt. Express* **9**(2), 717–727 (2018).
20. A. Dubois, K. Grieve, G. Moneron, R. Lecaque, L. Vabre, and C. Boccara, "Ultrahigh-resolution full-field optical coherence tomography," *Appl. Opt.* **43**(14), 2874–2883 (2004).
21. O. Thouvenin, K. Grieve, P. Xiao, C. Apelian, and A. C. Boccara, "En face coherence microscopy," *Biomed. Opt. Express* **8**(2), 622–639 (2017).
22. P. Xiao, M. Fink, and A. C. Boccara, "Full-field spatially incoherent illumination interferometry: a spatial resolution almost insensitive to aberrations," *Opt. Lett.* **41**(17), 3920–3923 (2016).
23. P. Mecê, P. Xiao, V. Mazlin, J. Scholler, K. Grieve, J.-A. Sahel, M. Fink, and C. Boccara, "Towards lens-based wavefront sensorless adaptive optics full-field oct for in-vivo retinal imaging (conference presentation)," in *Optical Coherence Tomography and Coherence Domain Optical Methods in Biomedicine XXIII*, vol. 10867 (International Society for Optics and Photonics, 2019), p. 1086722.

24. P. Mécê, J. Scholler, K. Groux, and C. Boccara, "High-resolution in-vivo human retinal imaging using full-field ocr with optical stabilization of axial motion," *Biomed. Opt. Express* **11**(1), 492–504 (2020).
25. P. Xiao, V. Mazlin, K. Grieve, J.-A. Sahel, M. Fink, and A. C. Boccara, "In vivo high-resolution human retinal imaging with wavefront-correctionless full-field ocr," *Optica* **5**(4), 409–412 (2018).
26. W. Sellmeier, "Zur erkarung der abnormen farbenfolge im spectrum einiger. substanzen," *Ann. Phys.* **219**(6), 272–282 (1871).
27. J. Scholler, V. Mazlin, O. Thouvenin, K. Groux, P. Xiao, J.-A. Sahel, M. Fink, C. Boccara, and K. Grieve, "Probing dynamic processes in the eye at multiple spatial and temporal scales with multimodal full field ocr," *Biomed. Opt. Express* **10**(2), 731–746 (2019).
28. R. F. Cooper, G. K. Aguirre, and J. I. Morgan, "Fully automated estimation of spacing and density for retinal mosaics," *Trans. Vis. Sci. Tech.* **8**(5), 26 (2019).
29. J. I. Yellott Jr, "Spectral analysis of spatial sampling by photoreceptors: topological disorder prevents aliasing," *Vision Res.* **22**(9), 1205–1210 (1982).
30. C. A. Curcio, K. R. Sloan, R. E. Kalina, and A. E. Hendrickson, "Human photoreceptor topography," *J. Comp. Neurol.* **292**(4), 497–523 (1990).
31. R. F. Cooper, M. A. Wilk, S. Tarima, and J. Carroll, "Evaluating descriptive metrics of the human cone mosaic," *Invest. Ophthalmol. Visual Sci.* **57**(7), 2992–3001 (2016).
32. K. M. Litts, R. F. Cooper, J. L. Duncan, and J. Carroll, "Photoreceptor-based biomarkers in aoslo retinal imaging," *Invest. Ophthalmol. Visual Sci.* **58**(6), BIO255 (2017).
33. A. Podoleanu, M. Seeger, G. Dobre, D. Webb, D. Jackson, and F. Fitzke, "Transversal and longitudinal images from the retina of the living eye using low coherence reflectometry," *J. Biomed. Opt.* **3**(1), 12 (1998).
34. H. Kolb, "Gross anatomy of the eye," in *Webvision: The Organization of the Retina and Visual System [Internet]*, (University of Utah Health Sciences Center, 2007).
35. D. T. Miller, J. Qu, R. S. Jonnal, and K. E. Thorn, "Coherence gating and adaptive optics in the eye," in *Coherence Domain Optical Methods and Optical Coherence Tomography in Biomedicine VII*, vol. 4956 (International Society for Optics and Photonics, 2003), pp. 65–72.
36. E. Gofas-Salas, P. Mécê, L. Mugnier, A. M. Bonnefois, C. Petit, K. Grieve, J. Sahel, M. Paques, and S. Meimon, "Near infrared adaptive optics flood illumination retinal angiography," *Biomed. Opt. Express* **10**(6), 2730–2743 (2019).
37. C. Lavia, P. Mécê, M. Nassisi, S. Bonnin, J. Marie-Louise, A. Couturier, A. Erginay, R. Tadayoni, and A. Gaudric, "Retinal capillary plexus pattern and density from fovea to periphery measured in healthy eyes with swept-source optical coherence tomography angiography," *Sci. Rep.* **10**(1), 1474 (2020).
38. J. Scholler, K. Groux, K. Grieve, C. Boccara, and P. Mécê, "Adaptive-glasses wavefront sensorless full-field ocr for high-resolution retinal imaging over a wide field-of-view," arXiv preprint arXiv:2007.04986 (2020).